Single-Molecule Imaging of Na$_v$1.6 on the Surface of Hippocampal Neurons Reveals Somatic Nanoclusters

Elizabeth J. Akin,[1,2,3] Laura Solé,[3] Ben Johnson,[2,3] Mohamed el Beheiry,[8] Jean-Baptiste Masson,[7,9] Diego Krapf,[5,6,*] and Michael M. Tamkun[1,2,3,4,*]

[1]Cell and Molecular Biology Graduate Program, [2]Molecular, Cellular and Integrative Neuroscience Program, [3]Department of Biomedical Sciences, [4]Department of Biochemistry and Molecular Biology, [5]School of Biomedical Engineering, and [6]Department of Electrical and Computer Engineering, Colorado State University, Fort Collins, Colorado; [7]Institut Pasteur, Decision and Bayesian Computation, Centre National de la Recherche Scientifique (CNRS) UMR 3525, Paris, France; [8]Physico-Chimie Curie, Institut Curie, Paris Sciences Lettres, CNRS UMR 168, Université Pierre et Marie Curie, Paris, France; and [9]Janelia Research Campus, Howard Hughes Medical Institute, Ashburn, Virginia

ABSTRACT Voltage-gated sodium (Na$_v$) channels are responsible for the depolarizing phase of the action potential in most nerve cells, and Na$_v$ channel localization to the axon initial segment is vital to action potential initiation. Na$_v$ channels in the soma play a role in the transfer of axonal output information to the rest of the neuron and in synaptic plasticity, although little is known about Na$_v$ channel localization and dynamics within this neuronal compartment. This study uses single-particle tracking and photoactivation localization microscopy to analyze cell-surface Na$_v$1.6 within the soma of cultured hippocampal neurons. Mean-square displacement analysis of individual trajectories indicated that half of the somatic Na$_v$1.6 channels localized to stable nanoclusters ~230 nm in diameter. Strikingly, these domains were stabilized at specific sites on the cell membrane for >30 min, notably via an ankyrin-independent mechanism, indicating that the means by which Na$_v$1.6 nanoclusters are maintained in the soma is biologically different from axonal localization. Nonclustered Na$_v$1.6 channels showed anomalous diffusion, as determined by mean-square-displacement analysis. High-density single-particle tracking of Na$_v$ channels labeled with photoactivatable fluorophores in combination with Bayesian inference analysis was employed to characterize the surface nanoclusters. A subpopulation of mobile Na$_v$1.6 was observed to be transiently trapped in the nanoclusters. Somatic Na$_v$1.6 nanoclusters represent a new, to our knowledge, type of Na$_v$ channel localization, and are hypothesized to be sites of localized channel regulation.

INTRODUCTION

Voltage-gated sodium (Na$_v$) channels are responsible for the initiation and conduction of most neuronal action potentials. Na$_v$ channels are composed of a large pore-forming α-subunit of ~1900 amino acids and smaller auxiliary β-subunits (1). Of the nine Na$_v$ α-subunits (Na$_v$1.1–1.9), Na$_v$1.1, Na$_v$1.2, Na$_v$1.3, and Na$_v$1.6 are the major isoforms within the central nervous system (2) where the differential expression and distribution of Na$_v$ isoforms within the somatodendritic and axonal compartments determine the action potential waveform (3–5). Thus, the number, type, and location of channels must be tightly regulated to ensure proper neuronal function. Na$_v$ localization to the axon initial

segment (AIS) has been extensively studied, since this domain is vital to action potential initiation (3,6–8). In contrast, little is known about Na$_v$ channel localization and dynamics within the neuronal cell body even though somatic Na$_v$ channels play a role in synaptic plasticity and in the transfer of axonal output information to the rest of the neuron (9,10).

Multiple studies have revealed that the cell surface is highly compartmentalized such that restricted movement and localization of surface proteins enhances signaling by altering diffusion-limited biochemical reactions (11–13). Furthermore, this compartmentalization is dynamic and highly regulated. Some of the best examples deal with the diffusion of neurotransmitter receptors into the postsynaptic membrane where they can become transiently tethered to intracellular scaffolds (14,15). For example, single-molecule studies of AMPA and glycine receptors indicate that receptor diffusion and tethering at the synapse can be highly

regulated (16–18). Whether similar diffusion patterns exist for other neuronal proteins, such as Na$_v$1.6, and within extrasynaptic compartments, is the focus of this study.

In addition to axon localization, Na$_v$ channels are present in both somatic and dendritic compartments, as demonstrated by functional methods including electrophysiology and fluorescent Na$^+$ indicators (4,10,19,20). Localized somatic application of sodium channel blockers diminishes action potential back-propagation, suggesting that these channels relay information about axon output to the rest of the neuron. In addition, somatic spiking has been postulated to regulate synaptic plasticity in the absence of back-propagating action potentials (9). Furthermore, there is precedence that Na$_v$ channels in the AIS and somatodendritic compartments are functionally distinct and differentially regulated. In neocortical neurons, slowly inactivating, persistent current is derived from AIS channels as opposed to those in the soma (21). Activation of D1/D5 dopamine receptors in prefrontal-cortex pyramidal neurons preferentially modulates Na$_v$ channels in the soma and proximal dendrites and increases the amount of persistent current (19). Despite the functional importance of Na$_v$ channels in the cell body, the distribution and dynamics of somatodendritic Na$_v$ channels has remained elusive because traditional immunofluorescence-based assays are not sensitive enough to detect the sparse Na$_v$ channel distribution in the soma (4,8,22). Quantitative electron microscopy using immunogold-labeled SDS-digested freeze-fracture replica labeling has so far provided the best demonstration that Na$_v$ channels are present on the soma and dendrites of hippocampal CA1 pyramidal cells, although at a density ~40 times lower than that in the AIS (23). However, this high-resolution approach provides no information concerning dynamics and potential interactions of Na$_v$ channels on the cell surface.

This article focuses on the surface localization and diffusion of Na$_v$1.6 channels on the soma of live rat hippocampal neurons. The Na$_v$1.6 isoform was chosen for our current studies because it is abundant in the central nervous system, may have location-specific biophysical properties, since it is present within both the somato-dendritic and axonal compartments, and is directly linked to human pathologies such as ataxia (24,25), epilepsy (26), multiple sclerosis (27), and stroke (28). Using fluorescent protein- and extracellular epitope-tagged Na$_v$1.6 constructs in conjunction with high-density single-particle tracking, we found that somatic Na$_v$1.6 channels localized to stable nanoclusters ~230 nm in diameter. The nanoscale organization of Na$_v$ channels was further elucidated by analyzing single-molecule trajectories via quantitative Bayesian inference methods. These nanoclusters were found to be ankyrin-, actin-, and clathrin-independent and, as such, represent a new type of molecular organization of Na$_v$ channels on the neuronal surface. We postulate that Na$_v$1.6 nanoclusters represent sites of channel regulation, potentially contrib-

uting to the functional differences seen between somatic and axonal Na$_v$ channels.

MATERIALS AND METHODS

Cell culture

Rat hippocampal neurons were cultured as previously described (29). Animals were used according to protocols approved by the Institutional Animal Care and Use Committee of Colorado State University (Animal Welfare Assurance Number A3572-01). Embryonic hippocampal tissue was collected after anesthesia with isoflurane followed by decapitation. E18 rat hippocampal neurons were plated on glass-bottom 35 mm dishes with No. 1.5 coverslips (MatTek, Ashland, MA) that were coated with poly-L-lysine (Sigma-Aldrich, St. Louis, MO). Neurons were grown in Neurobasal Medium (Gibco/Thermo Fisher Scientific, Waltham, MA) with penicillin/streptomycin antibiotics (Cellgro/Mediatech, Manassas, VA), GlutaMAX (Gibco/Thermo Fisher Scientific), and NeuroCult SM1 Neuronal Supplement (STEMCELL Technologies, Vancouver, BC, Canada). For imaging, the cultures were incubated in neuronal imaging saline consisting of 126 mM NaCl, 4.7 mM KCl, 2.5 mM CaCl$_2$, 0.6 mM MgSO$_4$, 0.15 mM NaH$_2$PO$_4$, 0.1 mM ascorbic acid, 8 mM glucose, and 20 mM HEPES (pH 7.4).

Transfection

Wild-type and mutant Na$_v$1.6 containing GFP and an extracellular biotin acceptor domain (BAD) (Na$_v$1.6-BAD-GFP and Na$_v$1.6-BAD-dABM) were constructed and functionally validated as previously described (29). Na$_v$1.6-Dendra2 was constructed by replacing the GFP from Na$_v$1.6-GFP with Dendra2 using KpnI and PacI restriction sites. Neuronal transfections were performed after days in vitro (DIV) 4–6 in culture as indicated for each experiment using Lipofectamine 2000 (Invitrogen, Life Technologies, Grand Island, NY) and either Na$_v$1.6-BAD, Na$_v$1.6-Dendra2, or Na$_v$1.6-BAD-GFP (1 μg), human β1 in pcDNA3.1Mygro(+), and rat β2 in pcDNA3.1VS-HisTopoTA, as indicated. For the Na$_v$1.6-BAD-GFP and Na$_v$1.6-BAD constructs, pSec-BirA (bacterial biotin ligase) was cotransfected to biotinylate the channel. Plasmids encoding clathrin-light-chain-GFP, K$_v$2.1-GFP, photoactivatable-GFP-actin, and Ruby-Lifeact were used as previously described (30,31).

Live-cell surface labeling

For experiments using the Na$_v$1.6 construct containing the extracellular BAD, labeling of the surface channel was performed before imaging. Neurons were rinsed with neuronal imaging saline to remove the Neurobasal media and then incubated for 10 min at 37°C with either streptavidin-conjugated Alexa Fluor 594 (Thermo Fisher Scientific) or CF640R-streptavidin (Biotium, Hayward, CA) diluted 1:1000 in neuronal imaging saline. Excess label was removed by rinsing with imaging saline. CF640R was used for far-red imaging instead of streptavidin-conjugated Alexa Fluor 647, since we found that the latter does not label Na$_v$1.6-BAD efficiently. Alexa Fluor 647 has a higher molecular weight than either Alexa Fluor 594 or CF640R, suggesting that the biotin within the BAD domain is only accessible to smaller dye conjugates. For single-particle tracking photoactivated localization microscopy (spt-PALM) and actin super-resolution experiments, 0.1 μm TetraSpeck beads (Thermo Fisher Scientific) were used as fiduciary markers to correct for drift. Beads were diluted 1:1000 in imaging saline and applied to the cultures for 10 min to place several beads within the field of view.

Microscopy

Total internal reflection fluorescence (TIRF) images were acquired using a Nikon Eclipse Ti fluorescence microscope equipped with a Perfect-Focus

system, a Nikon photoactivation unit (PAU), acousto-optic-tunable-filter (AOTF)-controlled 405, 488, 561, and 647 nm diode lasers, 100 mW each split equally between the TIRF and PAU pathways, an Andor iXon EMCCD DU-897 camera, and a Plan Apo TIRF 100×, NA 1.49 objective. Emission was collected through a filter wheel containing the appropriate bandpass filters. For excitation, an incident angle of 63° was used that gives an estimated penetration depth of 144 nm at a wavelength $\lambda = 488$ nm. Before TIRF imaging, differential interference contrast (DIC) and widefield fluorescence imaging were used to distinguish transfected neurons from the relatively flat glia. Neurons were readily identified based on the characteristic soma morphology and localization of Na$_v$1.6 to the axon initial segment. All imaging was performed at 37°C using a heated stage and objective heater.

Mobility of Na$_v$1.6 puncta

The stability of Na$_v$1.6 puncta was assessed using a custom algorithm implemented in LabView. First, puncta were identified using a Fourier bandpass filter followed by threshold segmentation. Then, we used the puncta in the first frame of the video as a mask for all subsequent images such that only puncta that survived the Fourier filter and threshold segmentation and overlapped with puncta in the first frame were analyzed. This image processing algorithm provided a tool to quantify the fraction of channels that remained confined to a diffraction-limited spot after a given imaging time.

Fluorescence recovery after photobleaching

Neurons transfected with Na$_v$1.6-BAD and the biotin ligase were labeled with CF640R before TIRF imaging. The cells were imaged every 5 s for 2 min to establish a baseline. The microscope PAU was used to apply high-intensity illumination to a small region of the soma membrane until the initial fluorescence was photobleached (~10 s). After photobleaching, images were acquired every 5 s for 30 min to observe fluorescence recovery. Time-lapse microscopy at a low rate minimized photobleaching during the recovery period.

Single-molecule tracking

DIV10 rat hippocampal neurons expressing biotinylated Na$_v$1.6-BAD or Na$_v$1.6-BAD-GFP were surface-labeled with SA-CF640R and imaged at 20 frames/s using TIRF microscopy as described above. Images were background subtracted and filtered using a Gaussian kernel with a standard deviation of 0.7 pixels in ImageJ. Tracking of individual fluorophores was performed in MATLAB using the U-track algorithm developed by Jaqaman et al. (32). Manual inspection confirmed accurate single-molecule detection and tracking. The tracks were corrected for drift using TetraSpeck beads as fiducial markers, with custom-written LabView codes.

Analysis of diffusion and potential energy landscapes

The dynamics of Na$_v$ channels were mapped on the cell surface in terms of their diffusion and potential energy by using high-density single-particle tracking of Na$_v$ channels labeled with photoactivatable fluorophores (33) in conjunction with InferenceMAP, a software package based on Bayesian inference (34). DIV10 rat hippocampal neurons expressing Na$_v$1.6-Dendra2 were imaged using TIRF microscopy as described above. Images of the unconverted Dendra2 fluorescence and DIC images of the neurons were acquired both pre- and postimaging. The image of the unconverted Dendra2 fluorescence confirmed that the neuronal membrane was within the TIRF excitation field. Dendra2 was photoconverted with a low-intensity 405 nm laser, and photoconverted molecules were excited, imaged, and

subsequently photobleached using the 561 nm laser (50 mW). The 405 laser intensity was adjusted in the range 0.05 to 0.5 mW such that an appropriate density of photoconverted Dendra2 molecules was present. Image sequences of 10,000 frames were acquired at 20 frames/s for each cell. Single-molecule tracks were assembled using U-track and analyzed with InferenceMAP.

RESULTS

Somatic Na$_v$1.6 has a heterogeneous distribution

Our previous studies of Na$_v$1.6 examined the directed trafficking of nascent channels to the AIS of hippocampal neurons (29). In these studies, we transfected cultured rat hippocampal neurons with a modified Na$_v$1.6 construct, Na$_v$1.6-BAD, that contained an extracellular biotin acceptor domain (BAD), thus allowing live-cell labeling of surface channels using streptavidin-conjugated fluorophores. Fig. 1 A shows DIC and TIRF images of a cultured hippocampal neuron transfected with Na$_v$1.6-BAD, labeled with streptavidin-conjugated CF640R. In addition to the expected high-density surface localization within the AIS, Na$_v$1.6 localized to small surface puncta on the soma. As illustrated by the higher magnification of the soma shown in Fig. 1 C, the somatic channels are distributed nonuniformly, with single channels being either dispersed across the surface or aggregated into bright nanoclusters as indicated by the white arrows. Note that the Fig. 1 C image represents a different time point from that in Fig. 1 B, thus accounting for the nonidentical Na$_v$1.6 localization patterns. The contrast in Fig. 1 C is enhanced to allow visualization of the nanoclusters, which are dim compared to the high density of Na$_v$1.6 within the AIS. We use the term nanocluster here to refer to nanoscale-sized static structures that are smaller than the traditional light microscopy diffraction limit and include at least two channels (see the data in Figs. 4 and 5 for nanocluster size). Single-channel intensities can be derived from freely diffusing particles very likely representing single Na$_v$1.6 channels bound to one fluorophore-labeled streptavidin. Using this approach, the number of channels per nanocluster was found to be in the range 2–20. However, the uncertainty associated with the extent of streptavidin binding to the biotinylated channels and the efficiency of channel biotinylation by the cotransfected biotin ligase makes it difficult to determine the exact number of channels within each nanocluster. In contrast to what was observed in neurons, Na$_v$1.6 nanoclustering was not seen in transfected glial cells present within the neuronal cultures (Fig. 1 F). In addition, the distribution of surface puncta intensities illustrated in Fig. S1 in the Supporting Material shows high-intensity values, i.e., Na$_v$1.6 nanoclusters, in neurons that are absent from glia. Thus, the nanoclustering is a function of the neuronal surface as opposed to being induced by the surface labeling or GFP moiety of the Na$_v$1.6 construct. Fig. 1 G shows time-lapse imaging that indicates that the nanoclusters are stably localized
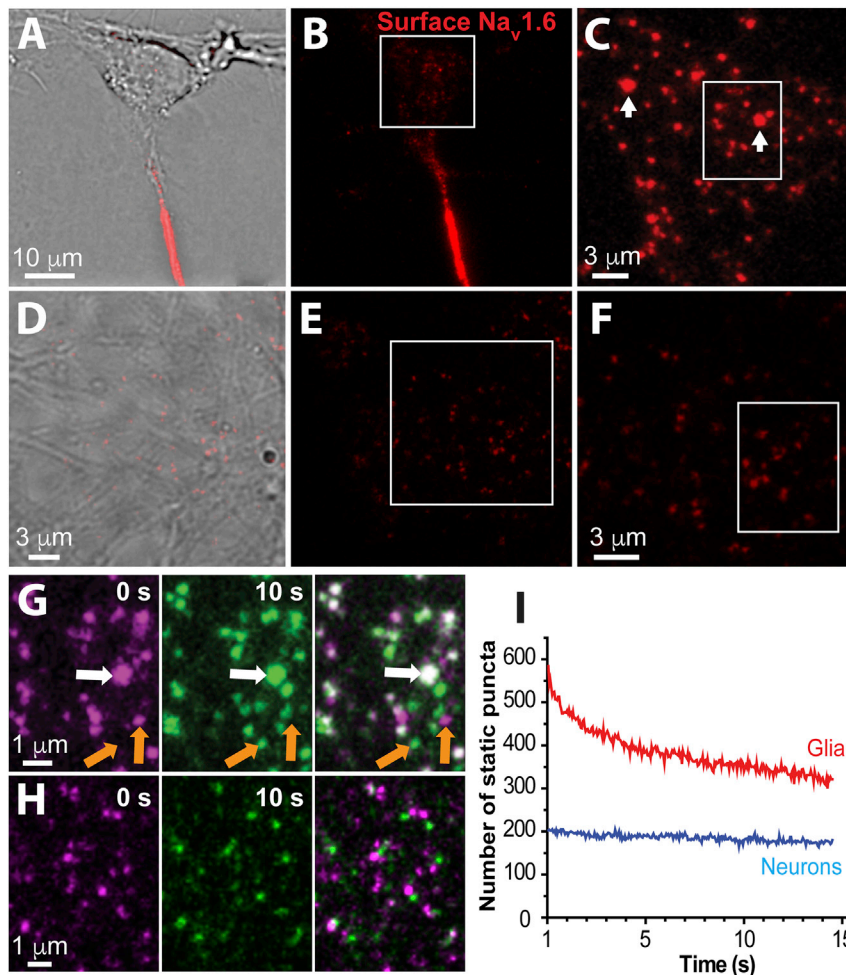
FIGURE 1 $Na_v1.6$ is distributed heterogeneously in the somatic membrane. (*A*) $Na_v1.6$-BAD surface expression in DIV10 rat hippocampal neurons is highly enriched at the AIS, as indicated by live-cell labeling with SA-CF640R (*red*). (*B*) Same image as (*A*) but without the DIC overlay. Channels on the somatic surface are barely visible at this contrast. (*C*) An enlargement of the boxed region shown in (*B*). The white arrows point to $Na_v1.6$-BAD surface nanoclusters. The image contrast is enhanced relative to that in (*B*) and a different time point is presented. (*D*) DIC and surface labeling of a transfected glial cell within the neuronal culture. (*E*) The surface expression pattern for $Na_v1.6$-BAD in the glial cell shown in (*D*). (*F*) An enlargement of the boxed region in (*E*). Note the absence of the neuronal nanoclusters. The heterogeneity in single-channel intensity is due to variability in CF640R labeling of the streptavidin in addition to single-fluorophore photobleaching during imaging. (*G*) *Left*: An enlargement of the white box in (*C*) with the CF640R fluorescence pseudocolored magenta. Contrast has been enhanced to visualize individual (*orange arrows*) and clustered (*white arrow*) somatic channels. *Middle*: The same field imaged 10 s later and with the SA-CF640R fluorescence now pseudocolored green. *Right*: Overlay of the two time frames, where colocalization appears white. The brightest punctum, i.e., nanocluster, appears in the same location in both image sequences (*white arrow*), whereas smaller puncta demonstrate mobility (*orange arrows*). (*H*) Same temporal analysis as in (*G*) but performed with the glial cell shown in (*D*)–(*F*). Note that most particles moved during the 10 s time period. (*I*) Stability of $Na_v1.6$ puncta. Puncta were detected in frame 1, and in subsequent frames the fraction of puncta remaining in the same location was determined. Summed data from three neurons and three glial cells are presented. The total puncta number in both cell types remained constant during this 15 s imaging period.

over at least 10 s on the neuronal surface, whereas the non-clustered channels are mobile. Fig. 1 *G*, *left*, pseudocolored in magenta, shows $t = 0$; Fig. 1 *G*, *middle*, pseudocolored in green, indicates $t = 10$ s; and Fig. 1 *G*, *right*, shows the merge of these frames. The presence of two channel populations, mobile and nanoclustered, is also evident in Movie S1. Interestingly, this image sequence suggests that $Na_v1.6$ can exchange between the nanoclusters and the mobile population. Note that the low intensity and mobile puncta in Movie S1 are interpreted as representing single channels. Fig. 1 *H* illustrates the enhanced mobility of $Na_v1.6$ channels that was observed in glial cells, where most of the channels are mobile. This enhanced movement is also illustrated in Movie S2. Occasionally static puncta were observed (*small white spots*), but none of these were nanoclusters in that the fluorescent intensity corresponded to only a single channel. Fig. 1 *I* summarizes the mobility of all surface channels in both neurons and glia. Here, all puncta (without discerning between single channels or nanoclusters) detected in frame 1 of movies from either glia or neurons

were analyzed as to whether they remained in their initial localization in subsequent frames. The number of puncta remaining in place relative to the first localization is plotted against time in Fig. 1 *I*. Note that in glia, the number of $Na_v1.6$ puncta that remained within the same location decreased much more rapidly than in neurons, indicating greater $Na_v1.6$ mobility relative to that observed in neurons. Photobleaching was minimal for the 15 s and the total number of detected puncta in each frame remained constant over this time.

$Na_v1.6$ somatic nanoclusters are ankyrin-G independent

The stable $Na_v1.6$ nanoclusters shown in Fig. 1 suggest $Na_v1.6$ interactions with an intracellular binding partner. The only known mechanism underlying Na_v localization in neurons involves cytoskeletal tethering via interactions with ankyrin-G (ankG) and loss of ankG-binding prevents localization of $Na_v1.6$ channels to the AIS without altering

channel function (35). To investigate the role of ankG-binding in the somatic nanoclustering of Na$_v$1.6, we examined the somatic distribution of a Na$_v$1.6 mutant channel in which the ankyrin-binding motif (ABM) was removed (Na$_v$1.6-BAD-dABM). We have previously shown that, in contrast to the wild-type channel (Fig.1), this ankyrin-G-binding mutant does not localize to the ankyrin-rich AIS (29). Fig. 2 shows a DIV10 neuron expressing Na$_v$1.6-BAD-dABM and ankG-GFP, which marks the AIS. In contrast to the wild-type channel that colocalizes with ankG at the AIS, the mutant channel does not concentrate within this region (29). However, Na$_v$1.6-BAD-dABM still localized to the somatic nanoclusters (Fig. 2 B). To visually display the mobility of nanoclusters and individual channels, we again overlaid two frames from an image sequence of channels labeled with CF640 on the somatic membrane (Fig. 2 B). When the first frame (Fig. 2 B, left) and a frame 10 s later (Fig. 2 B, middle) were overlaid we again saw that large puncta did not move over this time (white arrow),
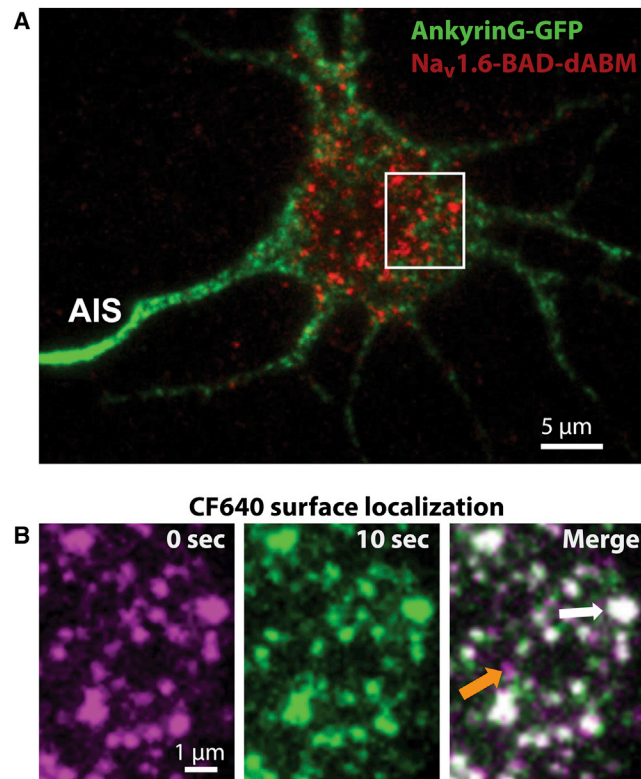
FIGURE 2 Na$_v$1.6 somatic distribution is ankyrin-G independent. (A) DIV10 rat hippocampal neuron expressing a mutant Na$_v$1.6 channel lacking the ankyrin-binding motif (Na$_v$1.6-BAD-dABM) labeled with CF640R. This channel localizes to the somatic region but does not show a high density of channels within the AIS, which is marked by ankyrin-G-GFP. (B) Enlargement of the area identified by the white box in (A), showing two frames of an image sequence spaced 10 s apart and a merged image (right). The first frame (magenta) and a frame 10 s later (green) are overlaid in the merged image. Colocalization appears white. Large bright puncta (white arrow) appear in the same location in both image sequences, whereas the smaller puncta are mobile (orange arrow).

whereas some of the smaller puncta (orange arrow), presumably single channels, did. Thus, the dABM mutant still produces both a mobile channel population and stable nanoclusters, similar to that seen for the full-length Na$_v$1.6 protein (Fig. 1 B). Since the somatic Na$_v$1.6 nanoclusters represent, to our knowledge, a new mechanism for Na$_v$ channel localization in a neuronal compartment where Na$_v$1.6 localization has not been previously appreciated, we next quantified the stability of these structures in greater detail.

Na$_v$1.6 localizes to stable somatic nanoclusters

To gain a quantitative understanding of nanocluster maintenance, we used time-lapse imaging and fluorescence recovery after photobleaching (FRAP). Fig. 3 A shows surface channels labeled with streptavidin-conjugated CF640 in a region within the soma. Three nanoclusters within the region of interest indicated by the dotted circle were photobleached. Then the cell was imaged for 30 min with images acquired at low frequency (every 5 s) to minimize photobleaching during fluorescence recovery. As illustrated in Fig. 3 A, very little recovery was seen for the bleached nanoclusters over this time frame. At 15 min (Fig. 3, A and B, third image), a small spot appeared at one of the bleached clusters and remained stationary over the next 15 min (orange arrows). Due to its low intensity relative to the unbleached nanoclusters, this spot most likely represents a single Na$_v$1.6 channel that diffused into this region and was captured into the nanocluster. This single-molecule recovery suggests that although exchange does occur between the clustered and nonclustered Na$_v$1.6 populations, it is relatively slow. Several of the bright puncta outside of the photobleached region persisted throughout the image sequence (Fig. 3 A, white arrows) suggesting that the Na$_v$1.6 somatic nanocluster domains are stably localized for more than 30 min. This assay is not sensitive to new channels being delivered to the plasma membrane (PM), since only the surface channels at the beginning of imaging were fluorescently labeled. Fig. 3 C shows the average fluorescence recovery of Na$_v$1.6 nanoclusters after photobleaching ($n = 5$ nanoclusters from three cells). Within 30 min measurements, the clusters are observed to recover 23% ± 9% (mean ± SD) of the original fluorescence intensity, indicating that in this timescale, only one in four original clustered channels is exchanged by surface diffusion.

Single-particle tracking of somatic Na$_v$1.6 channels

The data presented thus far imply that two populations of Na$_v$1.6 channels exist on the somatic surface, one being mobile and one stably anchored within nanoclusters. Although the ankG-independent nanocluster locations are stable over >30 min, there appears to be a slow exchange
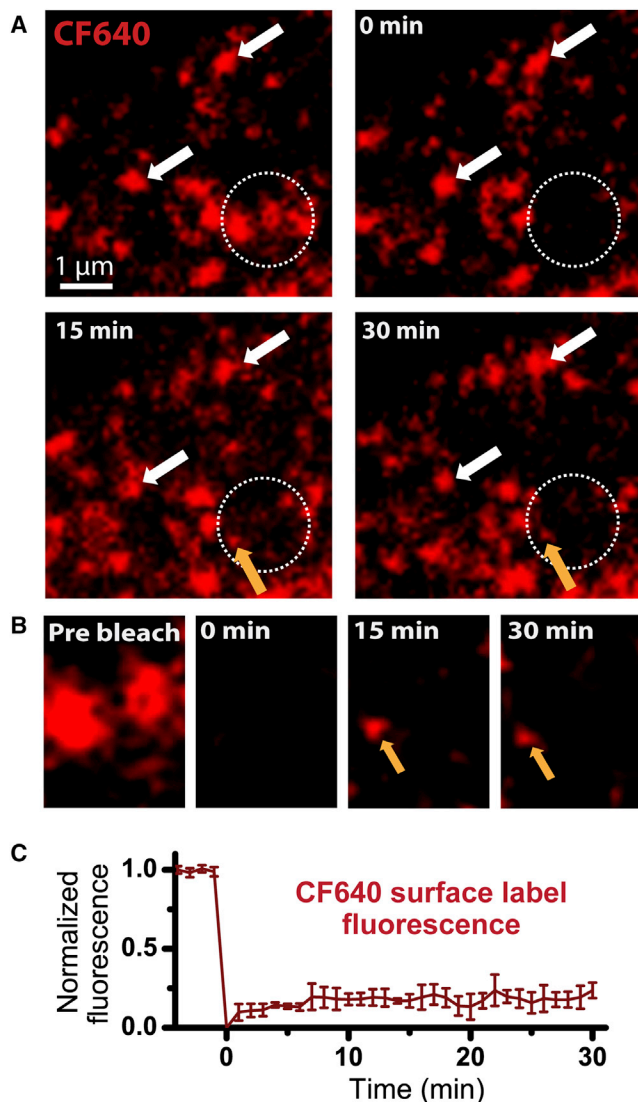
FIGURE 3 Na$_v$1.6 somatic nanoclusters are stable. Cell-surface Na$_v$1.6-BAD in DIV10 rat hippocampal neurons was detected with CF640. (*A*) A representative FRAP time course where the bleach was applied to the region of intereset indicated by the white dotted circle. Somatic nanoclusters outside of the bleached region show stable localization throughout the image sequence (*white arrows*). (*B*) Enlargement of a portion of the bleached region of interest in (*A*), showing fluorescence before photobleaching, immediately after photobleaching, and 15 and 30 min postbleach. Note the stable addition of a single Na$_v$1.6 channel at the 15 min time point (*orange arrows* in both *A* and *B*). (*C*) Average normalized FRAP over 30 min for CF640-labeled Na$_v$1.6 nanoclusters. On average, there was a 23% ± 9% (*n* = 5; mean ± SD) recovery. Fluorescence loss for channels outside of the bleached region during the experiment was <10%.

between the two populations, as illustrated in Fig. 3 *B*. To gain quantitative insights into the kinetics of Na$_v$1.6 channels, we examined the motion of somatic Na$_v$1.6 using single-particle tracking and analyzed 1478 trajectories in terms of their mean-square displacement (MSD). Fig. 4 *A* shows a set of trajectories obtained by imaging Na$_v$1.6 channels labeled with CF640R in an 8 μm × 11 μm window. The behavior of the trajectories is highly heterogeneous, with some molecules exploring large membrane regions and others showing tight confinement within small domains. The trajectories have been color-coded based on their associated diffusion coefficients, as discussed below.

The conventional way to characterize the mobility of individual molecules is by means of the time-averaged MSD, $\overline{\delta^2(t_{\text{lag}})}$,

$$\overline{\delta^2(t_{\text{lag}})} = \frac{1}{T - t_{\text{lag}}} \int_0^{T-t_{\text{lag}}} \left[\mathbf{r}(\tau + t_{\text{lag}}) - \mathbf{r}(\tau)\right]^2 d\tau,$$

where t_{lag} is the lag time, T the observation time, and $\mathbf{r}$ is the two-dimensional position of the particle. For particles undergoing Brownian motion, the MSD is linear in lag time. In particular, in two dimensions, $\overline{\delta^2(t_{\text{lag}})} = 4Dt_{\text{lag}}$. Thus, the MSD yields an effective diffusion coefficient. Fig. 4 *B* shows a histogram of effective diffusion coefficients obtained from a linear regression of the MSD at lag times up to 500 ms (10 frames). The effective diffusion coefficient is observed to have a broad distribution that spans more than two orders of magnitude. At least two populations are evident, a narrow peak at low diffusivities and a broad shoulder extending to large values. We placed trajectories into three different pools according to their effective diffusion coefficient using ad hoc thresholds, obtained from visual examination of the distribution. Namely, we arranged the trajectories into 1) a low-diffusivity regime with $D < 0.001$ μm^2/s, 2) an intermediate regime with 0.001 μm^2/s $< D < 0.03$ μm^2/s, and 3) a high-diffusivity regime. The low-diffusivity regime consists of 41% of the total trajectories, the intermediate regime 47%, and the high regime 11%. The trajectories in Fig. 4 *A* are colored red, blue, and green according to whether they have low, intermediate, or high diffusivity, respectively. As seen in the figure, the molecules with low diffusivity are strongly confined within nanoscale domains. The trajectories with intermediate diffusivity are partially confined, where part of the trajectory shows unconfined mobility. Usually the molecules exhibit intermittent behavior, alternating between phases of confinement and phases of unconfined diffusion. In some cases, the molecule is trapped again in the same domain from where it has escaped, and in others it is captured into a different domain. Lastly, the molecules in the high-diffusivity regime are not affected by the trapping domains and they do not exhibit any apparent confinement. Although this method of finding an effective diffusion coefficient is an efficient characterization tool for the mobility of the molecules, it does not necessarily represent the diffusion coefficient of the molecules given that it does not account for anomalous diffusion processes.

In addition to the diffusion coefficient, the MSD provides further information on protein dynamics. For example, a Brownian particle confined to a circular domain exhibits an MSD that is linear at short times but saturates at long
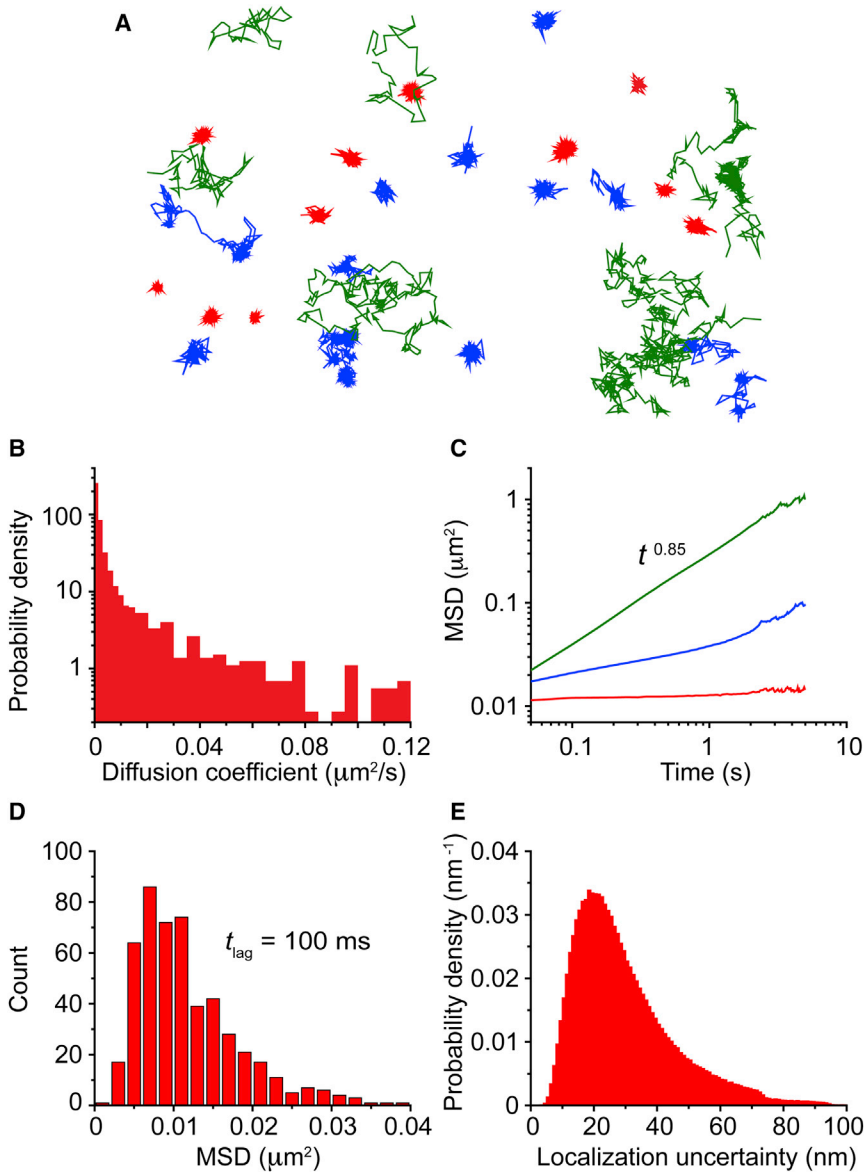
FIGURE 4 Single-molecule tracking reveals distinct distributions of somatic Na$_v$1.6 mobility. (*A*) Thirty-three representative single-molecule trajectories in an 8 μm $\times$ 11 μm window after surface labeling of Na$_v$1.6 with CF640 in DIV10 hippocampal neurons and tracking of individual channels. Imaging was performed at 20 Hz using TIRF microscopy. The red, blue, and green colors represent tracks with low, intermediate, or high diffusivity, respectively. (*B*) Histogram of effective diffusion coefficients of 1478 particles from four cells obtained from a linear regression of the MSD at lag times up to 500 ms (10 frames). (*C*) MSD as a function of lag time for three different populations. Trajectories were placed into three different pools according to their effective diffusion coefficients using ad hoc thresholds. Specifically, trajectories were placed into 1) a low-diffusivity regime, with $D < 0.001$ μm^2/s, 2) an intermediate regime, with 0.001 μm^2/s $< D < 0.03$ μm^2/s, and 3) a high-diffusivity regime. These three populations are color-coded as in (*A*). (*D*) Histogram of the MSDs at lag time t_{lag} = 100 ms for the trajectories in the low-diffusivity regime, which correspond to the molecules that remain confined during the whole observation time. (*E*) Distribution of localization uncertainty of all localized particles, from which $\sigma = 29 \pm 15$ nm (mean $\pm$ SD).

times such that $\overline{\delta^2} \sim R^2/2$, where R is the radius of the domain. Furthermore, the PM is often characterized by subdiffusive behavior (36,37), with $\overline{\delta^2}(t_{lag}) = K_\alpha t_{lag}^\alpha$, where K_α is the generalized diffusion coefficient with units cm^2/s$^\alpha$, and $\alpha < 1$ is the anomalous exponent. We expect different populations of Na$_v$ channels to be described by different types of MSDs. Fig. 4 *C* shows the MSD averaged for all trajectories within each diffusivity regime. In each of these regimes, the MSD has very distinctive features. For the molecules with low effective diffusion coefficient, the MSD rapidly converges to a value of $\overline{\delta^2} = 0.012$ μm^2/s, which is characteristic of confined particles. The high-diffusivity regime shows anomalous diffusion with $\alpha = 0.85$ during the whole observation time. On the other hand, the intermediate regime exhibits two different behaviors. At short lag times, the MSD appears to saturate, as in confined motion,

but at longer times, the MSD increases again. This behavior is expected for molecules that are transiently confined but are able to escape from the trapping environment until they are captured again into a new domain. The inflection point in the MSD indicates that the characteristic trapping time of these molecules is of the order of 1 s.

When particles are confined, the size of the domain can be estimated from the saturation in the MSD. Fig. 4 *D* shows a histogram of the MSDs at lag time $t_{lag} = 100$ ms for the trajectories in the low-diffusivity regime, which correspond to the molecules that remain confined during the whole observation time. The MSD at 100 ms, $\overline{\delta^2} = 0.012 \pm 0.009$ μm^2 (mean $\pm$ SD), is a good indicator of the saturation value. However, two different features can affect the MSD saturation, the radius of the domain and the localization error. In practice, $\overline{\delta^2} = R^2/2 + 4\sigma^2$, where σ is the localization standard error

and, assuming that the domain is circular, R is its radius. Fig. 4 E shows the distribution of localization uncertainty of all localized particles, from which we find $\sigma = 29 \pm 15$ nm (mean $\pm$ SD). Taking this localization uncertainty into account, we can infer the radii of the confinement domains to be $R = 130 \pm 90$ nm. Note that this size is at or below the diffraction limit of traditional imaging. Thus, size cannot be inferred from the images presented in Figs. 1, 2, and 3.

Diffusion and energy landscapes of Na$_v$1.6 on the soma

Considering that a subpopulation of channels is localized to stable nanocluster domains, we sought to map the two-dimensional diffusion and energy landscapes of Na$_v$1.6 channels using high-density single-particle tracking and Bayesian inference methods. A suitable method for measuring single-particle trajectories at high densities consists of labeling the molecules with photoactivatable fluorophores so that at any given time only a small fraction of the molecules are in their active fluorescence state. This technique, known as spt-PALM (33), allows the sampling of hundreds of thousands of short trajectories within a single cell. We used Na$_v$1.6 tagged with Dendra2 on the C-terminus (Na$_v$1.6-Dendra2). Dendra2 is a monomeric protein that emits green fluorescence in its unconverted state and irreversibly switches to red emission upon irradiation with violet light (38). Fig. 5 A shows a TIRF image of a rat
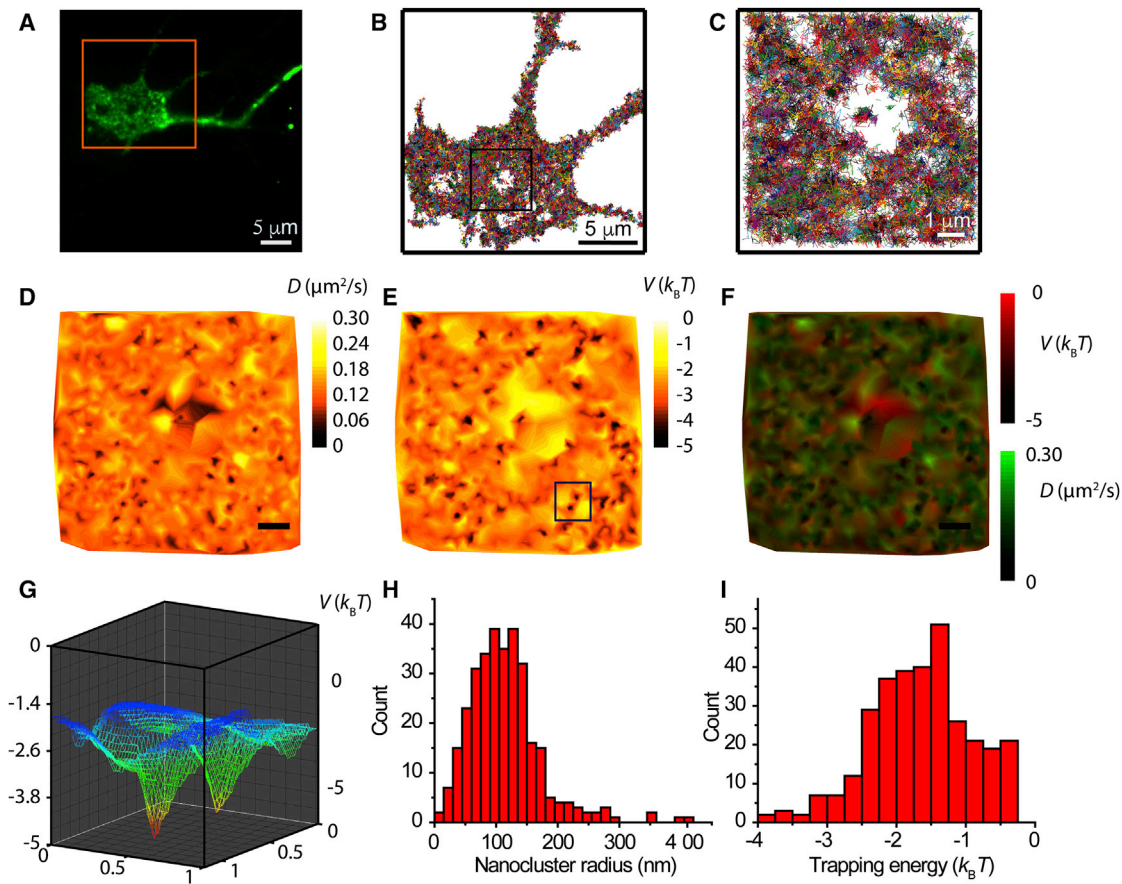

FIGURE 5 spt-PALM of Na$_v$1.6-Dendra2 shows heterogeneity in the diffusion and energy landscapes. (A) DIV 10 hippocampal neuron expressing Na$_v$1.6-Dendra2, showing unconverted Dendra2 as imaged in TIRF. (B) Ensemble of tracks from individual Na$_v$1.6-Dendra2 particles in the somatic region (orange box in (A)). Dendra2 particles were stochastically activated to allow visualization of individual particles while image sequences of 10,000 frames were acquired at 20 Hz. Molecules were detected and connected into tracks using U-track. Each colored line represents a track from an individual particle. The boxed region alone represents 114,923 Dendra2 detections. (C) An enlargement of the boxed region in (B). (D) Diffusion landscape of the membrane region illustrated in (C). The cell surface was divided into regions based on adaptive meshing, such that each section contains a similar number of localizations. The step sizes of particle tracks within these regions were used to determine the diffusion coefficient within each grid. (E) Potential energy landscape. Information about both the mobility of channels and the direction of movement were used to determine the potential energy. Energy wells appear as the dark puncta. (F) Overlay of the diffusion and potential energy maps. Dark spots indicate regions where both the energy and the diffusivity are lower than in the rest of the membrane. (G) 3D representation of the two energy wells indicated by the box in (E). (H) Distribution of energy well radii measured in 158 domains. The radius was defined as the standard deviation of the Gaussian fit and two radii were measured for each nanocluster, σ_x and σ_y. From the energy wells, the nanocluster radii were found to be 114 ± 58 nm (mean $\pm$ SD). (I) Distribution of the energy well depths. The measured trapping energy was -1.6 ± 0.7 k_BT.

hippocampal neuron expressing Na$_v$1.6-Dendra2, acquired with 488 nm excitation to observe the total expression before photoconversion. Here, the unconverted green Dendra2 shows all surface channels and fluorescence from any intracellular channels excited by the TIR excitation field. The surface-specific labeling shown in Fig. 1 B is sparse by comparison, due not only to the low surface density on the soma but also to the fact that channel biotinylation and streptavidin binding are not 100% efficient. Using a low-intensity 405 nm laser, a sparse subset of photoconverted molecules were continuously maintained in the field of view. The photoconverted molecules were imaged under 561 nm excitation and tracked until they photobleached. Fig. 5 B shows the tracks obtained from sptPALM during 8 min (10,000 frames), where each colored line represents a track from an individual photoconverted Dendra2 molecule. The precision of localization as determined by Gaussian fitting was $\sigma = 39 \pm 18$ nm. Further details can be observed in the 8 μm $\times$ 8 μm enlarged region shown in Fig. 5 C, defined by the dark square in Fig. 5 B. Note that the central region in Fig. 5 C that is devoid of single-molecule tracks most likely represents a part of the soma membrane that was not in direct contact with the coverslip surface and thus was outside the TIRF illumination field.

The high-density single-molecule data were used to obtain large-scale maps of the diffusivity and energy landscapes using InferenceMAP, an inference software based on Bayesian tools (34). Unsupervised learning was used to mesh the surface of cells according to local density. This strategy leads to a Voronoi tessellation of Na$_v$1.6 channel localization with higher resolution in dense regions such as nanocluster domains. Voronoi tessellation ensures a regularized amount of information spread over the complete surface of the cell. The diffusivity, D, and potential energy, V, of each subdomain are estimated from the displacements within the observed trajectories (39,40). The system is not assumed to be in thermodynamic equilibrium, and thus, the energy is computed from the molecular translocations and not from the channel density. Fig. 5 D shows the diffusivity map determined from the trajectories in Fig. 5 C. Although most of the surface has a diffusivity $D = 0.13 \pm 0.02$ μm^2/s, small dark pockets of lower diffusivity where $D < 0.06$ μm^2/s are apparent. Fig. 5, E and F, shows the potential energy landscape (E) and an overlay of diffusivity (*green*) and energy (*red*) (F). The energy landscape also exhibits lower energy wells where Na$_v$1.6 channels aggregate, i.e., at nanoclusters. The overlaid image shows many black spots where both the energy and the diffusivity are lower than in the rest of the membrane. These spots indicate that the diffusivity in the nanoclusters is smaller than that in the rest of the cell. Two energy wells, indicated by a box in Fig. 5 E, are shown in Fig. 5 G.

Given that the energy wells observed on the cell surface show the location and morphology of Na$_v$1.6 nanocluster domains, we took advantage of the energy landscape to map and characterize the nanoclusters in detail. The nanoclusters were identified by thresholding the energy landscape and then their size and energy depth were found by a Gaussian fit across the horizontal and vertical axes. We found an average of 3 nanoclusters/μm^2, but these domains were not uniformly distributed across the surface. Although some regions had a large concentration of nanoclusters, others seemed to be devoid of them. Fig. 5 H shows the distribution of nanocluster radii measured in 158 domains. The radius was defined as the standard deviation of the Gaussian fit and two radii were measured for each nanocluster, σ_x and σ_y. From the energy wells, the nanocluster radii were found to be 114 $\pm$ 58 nm (mean $\pm$ SD). This value agrees well with the 130 $\pm$ 90 nm radii of the confinement domains as determined from the MSD analysis of Fig. 4. Fig. 5 I shows the distribution of the depths of the energy wells. The measured trapping energy was found to be -1.6 ± 0.7 $k_B T$. Such a shallow energy depth is not consistent with molecules being confined within nanoclusters during long observation times as seen in Fig. 3. The discrepancy is due to the fact that all the molecules were employed to map the diffusion and energy landscapes, but only a molecular subpopulation (41%) were efficiently trapped into nanoclusters. Thus, although the trapped molecules allowed us to determine the nanocluster size with superior accuracy relative to the MSD analysis presented in Fig. 4, the nonclustering mobile molecules effectively lowered the calculated energy depth of the wells.

Na$_v$1.6 nanoclusters are actin independent

Since the localization mechanism of somatic Na$_v$1.6 is not due to ankyrin binding, we hypothesized that other cytoskeletal components may be involved. Indeed, actin regulates the formation of K$_v$2.1 K$^+$ channel domains in neurons (41) as well as the clustering of different membrane proteins in other cell types (42–44). Thus, we sought to determine whether Na$_v$1.6 nanoclusters are also stabilized by cortical actin. To this end, we imaged the cortical actin cytoskeleton with PALM superresolution while simultaneously observing Na$_v$1.6 localization. Actin was labeled with photoactivatable GFP and surface Na$_v$1.6 with CF640R. Superresolution imaging of F-actin as illustrated in Fig. S2 A failed to colocalize cortical actin filaments with the Na$_v$1.6 nanoclusters, although the two were often in close proximity. To further address whether actin is involved in Na$_v$1.6 localization, we imaged the distribution of Na$_v$1.6 in the presence of 200 nM swinholide A (swinA), a drug that both severs F-actin and sequesters G-actin (45). Fig. S3 shows that the intensity and location of the Na$_v$1.6 nanoclusters is not perturbed over 75 min after addition of swinA. Nanocluster number and location did not change after actin depolymerization ($p > 0.65$).

Na$_v$1.6 nanoclusters do not localize with clathrin-coated pits, mitochondria, or K$_v$2.1-induced endoplasmic-reticiulum-PM junctions

Since neither ankyrin-G nor actin seem to play an important role in the maintenance of the somatic nanoclusters, we next investigated whether Na$_v$1.6 colocalized with several scaffold/organelle markers. Since we have previously described that clathrin-coated pits transiently immobilize K$_v$2.1 K$^+$ channels (31), we coexpressed clathrin light chain tagged with GFP (CLC-GFP) with Na$_v$1.6. However, CLC-GFP did not colocalize with Na$_v$1.6-BAD nanoclusters labeled with CF640R (see Fig. S4 A), indicating that the nanoclusters are not clathrin-mediated endocytic platforms. This is consistent with the very long lifetime of the nanoclusters, since clathrin-coated pits are shorter-lived (seconds to minutes) (31,46). However, individual Na$_v$1.6 channels may interact with clathrin-coated pits for clathrin-mediated internalization.

Mitochondria, which localize near membrane-bound proteins and regulate them through calcium and oxidative signaling (47), were also evaluated as a candidate involved in the regulation of Na$_v$1.6 nanoclusters. MitoTracker-labeled mitochondria adjacent to the plasma membrane were imaged in TIRF mode and compared to the distribution of Na$_v$1.6-BAD labeled with streptavidin-AlexaFluor488. Again, no apparent relationship between mitochondria and the somatic nanoclusters was observed (Fig. S4 B).

We next looked at the correlation between Na$_v$1.6 nanoclusters and the delayed rectifier voltage-gated potassium channel, K$_v$2.1, which forms large, micron-sized clusters on both the soma and AIS of hippocampal neurons (48,49). These channels were recently found to mediate the formation of junctions between the endoplasmic reticulum and PM, which act as membrane trafficking hubs (50). As illustrated in Fig. S4 C, Na$_v$1.6-BAD nanoclusters were excluded from the large K$_v$2.1 clusters. This exclusion from K$_v$2.1-induced endoplasmic-reticulum-PM junctions is likely due to the large intracellular mass of the Na$_v$1.6 channel and may explain the small regions of soma membrane that were consistently devoid of Na$_v$1.6 single-molecule tracks, as illustrated in Fig. 5 C.

DISCUSSION

Due to the low numbers of somatic Na$_v$1.6 channels and lack of tools to visualize them, the cell surface distribution of this protein has not been previously visualized in living neurons. Here, with the use of Na$_v$1.6 constructs allowing the specific labeling of Na$_v$1.6 surface channels combined with the high sensitivity of TIRF microscopy, we were able to visualize with single-molecule sensitivity the compartmental distribution of somatic Na$_v$1.6 channels in live cells for the first time, to our knowledge. Specifically, we find a novel localization pattern of Na$_v$1.6 in cultured hippocampal neurons where channels are anchored within long-lived (>30 min) nanoclusters with radii of 114 nm. Nanoclustering was detected using three distinct experimental strategies, saturation labeling of all surface Na$_v$1.6 with fluorescent streptavidin (Fig. 1), single-particle tracking of a Na$_v$1.6 subpopulation labeled with fluorescent streptavidin (Fig. 4), and spt-PALM using a fluorescent protein tag without surface streptavidin labeling (Fig. 5). The consistency of the protein distribution between these methods argues that these structures are not an artifact of the fluorescent protein or epitope tagging of Na$_v$1.6, nor are they due to streptavidin labeling. In addition, the Na$_v$1.6 nanoclusters were not observed in glial cells, which suggests that Na$_v$1.6 nanoclustering is dependent on a protein or lipid component present in neurons but not glial cells. Importantly, Na$_v$ channel localization to these membrane domains is ankyrin independent, which is a striking discovery, since this is the only known ankyrin-independent mechanism for Na$_v$ channel localization in neurons.

The detection of Na$_v$1.6 channel localization with single-molecule sensitivity in living cells enabled analysis of channel mobility. This is important, since both location and dynamics provide insights into protein regulation, for tethering into macromolecular complexes and molecular encounters govern most biological signaling. Our current understanding is that the plasma membrane is structured such that molecular movement is influenced in a manner that increases the likelihood of relevant biochemical interactions. This organization is achieved through several different mechanisms, including compartmentalization by the actin cytoskeleton and protein-protein interactions, as well as through effects of local lipid environments (36). Our analysis of long trajectories provides information on the heterogeneity of individual Na$_v$1.6 behavior that is lost in ensemble techniques such as FRAP. Using spt-PALM data in combination with Bayesian inference tools, we were able to describe the diffusion and potential energy landscapes both surrounding and within stable membrane nanostructures. The strength of this approach lies in its ability to investigate the entire population of Na$_v$1.6 surface protein within a substantial timescale (8 min) and with high resolution.

Three distinct behaviors were observed in the dynamics of somatic Na$_v$1.6 channels. Single-particle tracking data indicate that 41% of channels are efficiently confined within nanoclusters for long times and a second population (11%) diffuses freely without interacting with the nanoclusters. Also apparent in the single-molecule data is a third population (47%) for which capturing interactions are weak and thus result in transient confinements. These observations suggest that Na$_v$1.6 channels undergo posttranslational modifications that alter interactions and localization within the plasma membrane.

We hypothesize that functional differences exist between clustered and nonclustered channels, perhaps in a fashion

similar to the behavior of K$_v$2.1 channels where clustered channels are held in a nonconducting state (51). Thus, modifications that regulate Na$_v$1.6 clustering would allow the effective regulation of Na$_v$1.6 function without the need of protein internalization to reduce voltage-dependent Na$^+$ currents. Alternatively, clustered Na$_v$1.6 channels could have biophysical properties distinct from the mobile population. Another possibility is that nanoclustering is linked to the function of other ion channels such as Na$^+$-dependent K$^+$ channels. Na$_v$1.6-dependent Na$^+$ influx is likely to only activate Na$^+$-dependent K$^+$ channel activity if the two channels are in very close proximity (52,53). However, it is possible that Na$_v$1.6 nanoclustering exists simply to enhance signaling fidelity. Theoretical work has demonstrated that 5–10 signaling molecules within a nanocluster can achieve an optimal signal/noise ratio by digitizing an analog signal (54). The physiological role of Na$_v$ channels is to transduce the analog-based membrane potential into the digital action potential. When Na$_v$ channels are clustered, it becomes much more likely that depolarizing stimuli will generate an action potential, for the localized depolarization caused by a single channel opening is more likely to activate other channels in its close vicinity before being dissipated.

What could be the mechanism responsible for the stable nanoclustering of Na$_v$1.6? The channels appear to be corralled within 114- to 130-nm-radius domains, which suggests an interaction with the cortical cytoskeleton. However, the actin cytoskeleton is not involved, given the actin imaging and depolymerization experiments shown in Figs. S2 and S3. It is possible that cytoplasmic regions of Na$_v$1.6 tether to intracellular scaffolds such as the recently described Kidins220/ARMS scaffolding protein that interacts with Na$_v$1.2 and modulates its activity (55). Alternatively, another possible mechanism involves Na$_v$1.6 glycosylation. Indeed, in Chinese hamster ovary cell lines expressing a dendritic cell membrane receptor (DC-SIGN), N-linked glycan-mediated interactions influence the overall lateral mobility of the protein (12). Na$_v$ channels can carry up to 40% of their mass in extracellular carbohydrate (56), and glycosylation is required for stable surface expression (57). Perhaps interaction of Na$_v$1.6 carbohydrate with extracellular structures influences the surface distribution in a fashion analogous to cytoskeletal interactions.

CONCLUSIONS

Despite the fact that Na$_v$ channels were discovered decades ago and their central importance to neuronal function has been long accepted, knowledge of Na$_v$ cell biology is surprisingly lacking relative to that regarding other ion channels. This has been especially true for the Na$_v$1.6 isoform that is perhaps the most abundant Na$_v$ channel in the mammalian brain. Our current study provides insight into the dynamics of Na$_v$1.6 on the cell surface and raises new questions such as how somatic localization and function are linked and how localized regulation of these channels may influence overall neuronal physiology. Importantly, understanding the complex diffusion and energy landscape of the neuronal surface is essential to furthering our understanding of basic neuronal cell biology and the molecular regulation of electrical activity in the brain.

SUPPORTING MATERIAL

Supporting Materials and Methods, four figures and two movies are available at http://www.biophysj.org/biophysj/supplemental/S0006-3495(16)30704-4.

AUTHOR CONTRIBUTIONS

ACKNOWLEDGMENTS

SUPPORTING CITATIONS

References 58,59 appear in the Supporting Material.

REFERENCES

1. Isom, L. L., K. S. De Jongh, …, W. A. Catterall. 1992. Primary structure and functional expression of the β1 subunit of the rat brain sodium channel. *Science.* 256:839–842.

2. Catterall, W. A., A. L. Goldin, and S. G. Waxman. 2005. International Union of Pharmacology. XLVII. Nomenclature and structure-function relationships of voltage-gated sodium channels. *Pharmacol. Rev.* 57:397–409.

3. Boiko, T., A. Van Wart, …, G. Matthews. 2003. Functional specialization of the axon initial segment by isoform-specific sodium channel targeting. *J. Neurosci.* 23:2306–2313.

4. Hu, W., C. Tian, …, Y. Shu. 2009. Distinct contributions of Na$_v$1.6 and Na$_v$1.2 in action potential initiation and backpropagation. *Nat. Neurosci.* 12:996–1002.

5. Lorincz, A., and Z. Nusser. 2008. Cell-type-dependent molecular composition of the axon initial segment. *J. Neurosci.* 28:14329–14340.

6. Zhou, D., S. Lambert, …, V. Bennett. 1998. AnkyrinG is required for clustering of voltage-gated Na channels at axon initial segments and for normal action potential firing. *J. Cell Biol.* 143:1295–1304.

7. Meeks, J. P., and S. Mennerick. 2007. Action potential initiation and propagation in CA3 pyramidal axons. *J. Neurophysiol.* 97:3460–3472.

8. Kole, M. H., S. U. Ilschner, …, G. J. Stuart. 2008. Action potential generation requires a high sodium channel density in the axon initial segment. *Nat. Neurosci.* 11:178–186.

9. Myoga, M. H., M. Beierlein, and W. G. Regehr. 2009. Somatic spikes regulate dendritic signaling in small neurons in the absence of backpropagating action potentials. *J. Neurosci.* 29:7803–7814.

10. Williams, S. R., and G. J. Stuart. 2000. Action potential backpropagation and somato-dendritic distribution of ion channels in thalamocortical neurons. *J. Neurosci.* 20:1307–1317.

11. Cambi, A., M. Lakadamyali, …, M. F. Garcia-Parajo. 2013. Meeting report—Visualizing signaling nanoplatforms at a higher spatiotemporal resolution. *J. Cell Sci.* 126:3817–3821.

12. Torreno-Pina, J. A., B. M. Castro, …, M. F. Garcia-Parajo. 2014. Enhanced receptor-clathrin interactions induced by N-glycan-mediated membrane micropatterning. *Proc. Natl. Acad. Sci. USA.* 111:11037–11042.

13. Torreno-Pina, J. A., C. Manzo, …, M. F. Garcia-Parajo. 2016. The actin cytoskeleton modulates the activation of iNKT cells by segregating CD1d nanoclusters on antigen-presenting cells. *Proc. Natl. Acad. Sci. USA.* 113:E772–E781.

14. Choquet, D., and A. Triller. 2013. The dynamic synapse. *Neuron.* 80:691–703.

15. Kneussel, M., A. Triller, and D. Choquet. 2014. SnapShot: receptor dynamics at plastic synapses. *Cell.* 157:1738.

16. Renner, M., C. Schweizer, …, S. Lévi. 2012. Diffusion barriers constrain receptors at synapses. *PLoS One.* 7:e43032.

17. Rust, M. B., C. B. Gurniak, …, W. Witke. 2010. Learning, AMPA receptor mobility and synaptic plasticity depend on n-cofilin-mediated actin dynamics. *EMBO J.* 29:1889–1902.

18. Specht, C. G., N. Grünewald, …, A. Triller. 2011. Regulation of glycine receptor diffusion properties and gephyrin interactions by protein kinase C. *EMBO J.* 30:3842–3853.

19. Gorelova, N., and J. K. Seamans. 2015. Cell-attached single-channel recordings in intact prefrontal cortex pyramidal neurons reveal compartmentalized D1/D5 receptor modulation of the persistent sodium current. *Front. Neural Circuits.* 9:4.

20. Fleidervish, I. A., N. Lasser-Ross, …, W. N. Ross. 2010. Na$^+$ imaging reveals little difference in action potential-evoked Na$^+$ influx between axon and soma. *Nat. Neurosci.* 13:852–860.

21. Astman, N., M. J. Gutnick, and I. A. Fleidervish. 2006. Persistent sodium current in layer 5 neocortical neurons is primarily generated in the proximal axon. *J. Neurosci.* 26:3465–3473.

22. Tian, C., K. Wang, …, Y. Shu. 2014. Molecular identity of axonal sodium channels in human cortical pyramidal cells. *Front. Cell. Neurosci.* 8:297.

23. Lorincz, A., and Z. Nusser. 2010. Molecular identity of dendritic voltage-gated sodium channels. *Science.* 328:906–909.

24. Sharkey, L. M., X. Cheng, …, M. H. Meisler. 2009. The ataxia3 mutation in the N-terminal cytoplasmic domain of sodium channel Na$_v$1.6 disrupts intracellular trafficking. *J. Neurosci.* 29:2733–2741.

25. Trudeau, M. M., J. C. Dalton, …, M. H. Meisler. 2006. Heterozygosity for a protein truncation mutation of sodium channel SCN8A in a patient with cerebellar atrophy, ataxia, and mental retardation. *J. Med. Genet.* 43:527–530.

26. Meisler, M. H., and J. A. Kearney. 2005. Sodium channel mutations in epilepsy and other neurological disorders. *J. Clin. Invest.* 115:2010–2017.

27. Craner, M. J., J. Newcombe, …, S. G. Waxman. 2004. Molecular changes in neurons in multiple sclerosis: altered axonal expression of Nav1.2 and Nav1.6 sodium channels and Na$^+$/Ca^{2+} exchanger. *Proc. Natl. Acad. Sci. USA.* 101:8168–8173.

28. Hinman, J. D., M. N. Rasband, and S. T. Carmichael. 2013. Remodeling of the axon initial segment after focal cortical and white matter stroke. *Stroke.* 44:182–189.

29. Akin, E. J., L. Solé, …, M. M. Tamkun. 2015. Preferential targeting of Nav1.6 voltage-gated Na$^+$ channels to the axon initial segment during development. *PLoS One.* 10:e0124397.

30. Fox, P. D., C. J. Haberkorn, …, M. M. Tamkun. 2013. Plasma membrane domains enriched in cortical endoplasmic reticulum function as membrane protein trafficking hubs. *Mol. Biol. Cell.* 24:2703–2713.

31. Weigel, A. V., M. M. Tamkun, and D. Krapf. 2013. Quantifying the dynamic interactions between a clathrin-coated pit and cargo molecules. *Proc. Natl. Acad. Sci. USA.* 110:E4591–E4600.

32. Jaqaman, K., D. Loerke, …, G. Danuser. 2008. Robust single-particle tracking in live-cell time-lapse sequences. *Nat. Methods.* 5:695–702.

33. Manley, S., J. M. Gillette, …, J. Lippincott-Schwartz. 2008. High-density mapping of single-molecule trajectories with photoactivated localization microscopy. *Nat. Methods.* 5:155–157.

34. El Beheiry, M., M. Dahan, and J. B. Masson. 2015. InferenceMAP: mapping of single-molecule dynamics with Bayesian inference. *Nat. Methods.* 12:594–595.

35. Gasser, A., T. S.-Y. Ho, …, S. D. Dib-Hajj. 2012. An ankyrinG-binding motif is necessary and sufficient for targeting Nav1.6 sodium channels to axon initial segments and nodes of Ranvier. *J. Neurosci.* 32:7232–7243.

36. Krapf, D. 2015. Mechanisms underlying anomalous diffusion in the plasma membrane. *Curr. Top. Membr.* 75:167–207.

37. Metzler, R., J. H. Jeon, …, E. Barkai. 2014. Anomalous diffusion models and their properties: non-stationarity, non-ergodicity, and ageing at the centenary of single particle tracking. *Phys. Chem. Chem. Phys.* 16:24128–24164.

38. Chudakov, D. M., S. Lukyanov, and K. A. Lukyanov. 2007. Tracking intracellular protein movements using photoswitchable fluorescent proteins PS-CFP2 and Dendra2. *Nat. Protoc.* 2:2024–2032.

39. Masson, J.-B., P. Dionne, …, M. Dahan. 2014. Mapping the energy and diffusion landscapes of membrane proteins at the cell surface using high-density single-molecule imaging and Bayesian inference: application to the multiscale dynamics of glycine receptors in the neuronal membrane. *Biophys. J.* 106:74–83.

40. Türkcan, S., A. Alexandrou, and J. B. Masson. 2012. A Bayesian inference scheme to extract diffusivity and potential fields from confined single-molecule trajectories. *Biophys. J.* 102:2288–2298.

41. O'Connell, K. M., A. S. Rolig, …, M. M. Tamkun. 2006. K$_v$2.1 potassium channels are retained within dynamic cell surface microdomains that are defined by a perimeter fence. *J. Neurosci.* 26:9609–9618.

42. Bakker, G. J., C. Eich, …, M. F. Garcia-Parajo. 2012. Lateral mobility of individual integrin nanoclusters orchestrates the onset for leukocyte adhesion. *Proc. Natl. Acad. Sci. USA.* 109:4869–4874.

43. Goswami, D., K. Gowrishankar, …, S. Mayor. 2008. Nanoclusters of GPI-anchored proteins are formed by cortical actin-driven activity. *Cell.* 135:1085–1097.

44. van Zanten, T. S., A. Cambi, …, M. F. Garcia-Parajo. 2009. Hotspots of GPI-anchored proteins and integrin nanoclusters function as nucleation sites for cell adhesion. *Proc. Natl. Acad. Sci. USA.* 106:18557–18562.

45. Bubb, M. R., I. Spector, …, E. D. Korn. 1995. Swinholide A is a microfilament disrupting marine toxin that stabilizes actin dimers and severs actin filaments. *J. Biol. Chem.* 270:3463–3466.

46. Loerke, D., M. Mettlen, …, S. L. Schmid. 2009. Cargo and dynamin regulate clathrin-coated pit maturation. *PLoS Biol.* 7:e57.

47. Chaplin, N. L., M. Nieves-Cintrón, …, G. C. Amberg. 2015. Arterial smooth muscle mitochondria amplify hydrogen peroxide microdomains functionally coupled to L-type calcium channels. *Circ. Res.* 117:1013–1023.

48. Sarmiere, P. D., C. M. Weigle, and M. M. Tamkun. 2008. The K$_v$2.1 K$^+$ channel targets to the axon initial segment of hippocampal and cortical neurons in culture and in situ. *BMC Neurosci.* 9:112.

49. Tamkun, M. M., K. M. O'Connell, and A. S. Rolig. 2007. A cytoskeletal-based perimeter fence selectively corrals a sub-population of cell surface K$_v$2.1 channels. *J. Cell Sci.* 120:2413–2423.

50. Fox, P. D., C. J. Haberkorn, …, M. M. Tamkun. 2015. Induction of stable ER-plasma-membrane junctions by K$_v$2.1 potassium channels. *J. Cell Sci.* 128:2096–2105.

51. O'Connell, K. M., R. Loftus, and M. M. Tamkun. 2010. Localization-dependent activity of the Kv2.1 delayed-rectifier K$^+$ channel. *Proc. Natl. Acad. Sci. USA.* 107:12351–12356.

52. Hage, T. A., and L. Salkoff. 2012. Sodium-activated potassium channels are functionally coupled to persistent sodium currents. *J. Neurosci.* 32:2714–2721.

53. Salkoff, L., A. Butler, …, A. Wei. 2006. High-conductance potassium channels of the SLO family. *Nat. Rev. Neurosci.* 7:921–931.

54. Roob, E., 3rd, N. Trendel, …, A. Mugler. 2016. Cooperative clustering digitizes biochemical signaling and enhances its fidelity. *Biophys. J.* 110:1661–1669.

55. Cesca, F., A. Satapathy, …, J. Scholz-Starke. 2015. Functional interaction between the scaffold protein Kidins220/ARMS and neuronal voltage-gated Na$^+$ channels. *J. Biol. Chem.* 290:18045–18055.

56. Marban, E., T. Yamagishi, and G. F. Tomaselli. 1998. Structure and function of voltage-gated sodium channels. *J. Physiol.* 508:647–657.

57. Waechter, C. J., J. W. Schmidt, and W. A. Catterall. 1983. Glycosylation is required for maintenance of functional sodium channels in neuroblastoma cells. *J. Biol. Chem.* 258:5117–5123.

58. Ovesný, M., P. Křížek, …, G. M. Hagen. 2014. ThunderSTORM: a comprehensive ImageJ plug-in for PALM and STORM data analysis and super-resolution imaging. *Bioinformatics.* 30:2389–2390.

59. Riedl, J., A. H. Crevenna, …, R. Wedlich-Soldner. 2008. Lifeact: a versatile marker to visualize F-actin. *Nat. Methods.* 5:605–607.

Supplemental Information

Single-Molecule Imaging of Na$_v$1.6 on the Surface of Hippocampal Neurons Reveals Somatic Nanoclusters

Elizabeth J. Akin, Laura Solé, Ben Johnson, Mohamed el Beheiry, Jean-Baptiste Masson, Diego Krapf, and Michael M. Tamkun

MATERIALS AND METHODS

Actin PALM imaging

We simultaneously imaged actin with super-resolution by PALM and cell surface $Na_v1.6$-BAD labeled with CF640R. Neurons were transfected with $Na_v1.6$-BAD and photoactivatable-GFP-actin (paGFP-actin). Before TIRF-based imaging, $Na_v1.6$-BAD was labeled with SA-CF640R and the cells then sequentially fixed with 0.3% glutaraldehyde for 1 min and 2% glutaraldehyde for 10 min prior to an incubation with 0.1% $NaBH_4$ for 7 min to reduce the fluorescence background. The channels were first imaged to determine their surface distribution. PALM was then used to localize single actin molecules in close proximity to the plasma membrane, i.e. within the TIRF excitation field. paGFP was converted from its non-fluorescent state to the fluorescent state using the 405nm-laser and the activated molecules were visualized and subsequently photobleached using high intensity 488 nm laser light. All the laser lines were maintained in TIRF to photoconvert and image only at the basal surface. Super-resolution images of actin localization were reconstructed using the ImageJ plugin ThunderSTORM (1). TIRF images of surface $Na_v1.6$-BAD (non-super-resolution) were overlaid on the super-resolution image of actin. TetraSpeck beads were used as fiduciary markers to correct for drift.

Actin depolymerization

Neurons were transfected with $Na_v1.6$-BAD and Ruby-Lifeact (gift from Dr. James Bamburg, Colorado State University). The surface distribution of $Na_v1.6$-BAD was again visualized with SA-CF640R. Transfected neurons were imaged in TIRF at one Hz for ~10 min to establish a baseline. SwinholideA (200 nM) was then added to the bath and actin depolymerization

monitored via Ruby-Lifeact. Neurons were imaged every 1 min for an additional hour to

determine the effect of actin depolymerization on $Na_v1.6$-BAD distribution.

RESULTS

Distribution of $Na_v1.6$ surface puncta intensities in neurons and glia

$Na_v1.6$-BAD was transfected into neuronal cultures and the surface-labeled channels were

imaged using TIRF microscopy. The measurement of $Na_v1.6$-BAD surface puncta fluorescence

intensities in neurons and glia allowed for a comparison of the surface distribution between these

cell types. The distribution of surface puncta intensities illustrated in Fig. S1 shows high

intensity values, i.e. $Na_v1.6$ nanoclusters, in neurons that are absent from glia. These results

suggest that nanoclustering of $Na_v1.6$ is cell-type specific.

SUPPLEMENTARY FIGURE 1 Histogram of puncta intensities for both neurons and glia. Cell surface $Na_v1.6$ was labeled with SA-CF640R and the fluorescence intensity of individual surface puncta, representing both single channels and channel aggregates, was measured. Summed data from three neurons and three glial cells are presented.
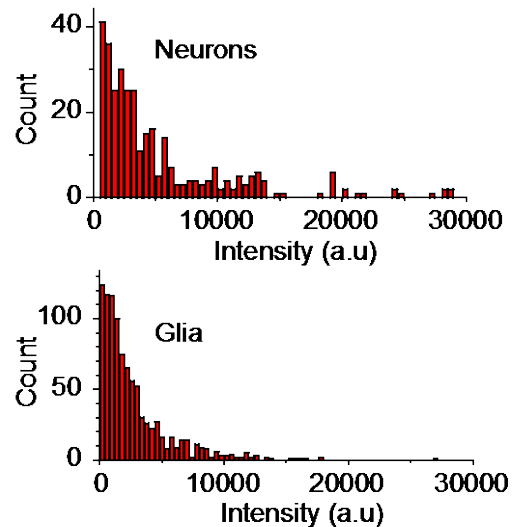
**$Na_v1.6$ nanoclusters are actin independent**

Since the localization mechanism of somatic

$Na_v1.6$ is not due to ankyrin-binding, we hypothesized that other cytoskeletal components may

be involved. Indeed, actin is involved in the localization of $K_v2.1$ to large, micron size clusters

on the soma of some neurons (2) as well as influencing the diffusion of a number of membrane

proteins. Thus we wanted to determine whether Na$_v$1.6 nanoclusters are also stabilized by cortical actin. Actin is present throughout nearly the entire neuron, while Na$_v$1.6 nanoclusters represent a very small fraction of the neuronal membrane. In order to determine whether there is any distinct actin organization present around the Na$_v$1.6 nanoclusters we used super-resolution microscopy such that actin molecules could be resolved below the diffraction limit. For this, we used photoactivation localization microscopy (PALM) of photoactivatable-GPF actin (paGFP-actin). Neurons were co-transfected with Na$_v$1.6-BAD and paGFP-actin and the Na$_v$1.6 surface distribution was visualized with SA-CF640. The 405-nm laser was used to activate low numbers of the paGFP-actin molecules, and the 488-nm laser was used to visualize and photobleach activated particles. Activated fluorophores were fit with a Gaussian distribution to localize particles. The localizations from each frame were reconstructed into a super-resolution image of the cortical actin for a DIV11 rat hippocampal neuron.

The image acquired using standard TIRF microscopy is displayed on the left side of Fig. S2A and the super-resolution reconstruction on the right. Fig. S2B shows an enlargement of the white box in Fig. S2A to demonstrate the relative distribution of Na$_v$1.6 and actin. Again, the image obtained by standard TIRF microscopy shows little fine structure (top panel), while PALM-based super-resolution clarifies the location of the actin (middle panel). Somatic Na$_v$1.6 channel nanoclusters localize to membrane regions distinct from, but often adjacent to, cortical actin structures present in the TIRF field (yellow arrows, middle and bottom panels). This spatial relationship is further demonstrated by the line scan in Fig. S2C, which is derived from the normalized fluorescence intensity of actin and surface-labeled Na$_v$1.6-BAD along the dotted line in Fig. S2A. While the cortical actin filaments did not localize with the Na$_v$1.6 nanoclusters the two were often in close proximity.
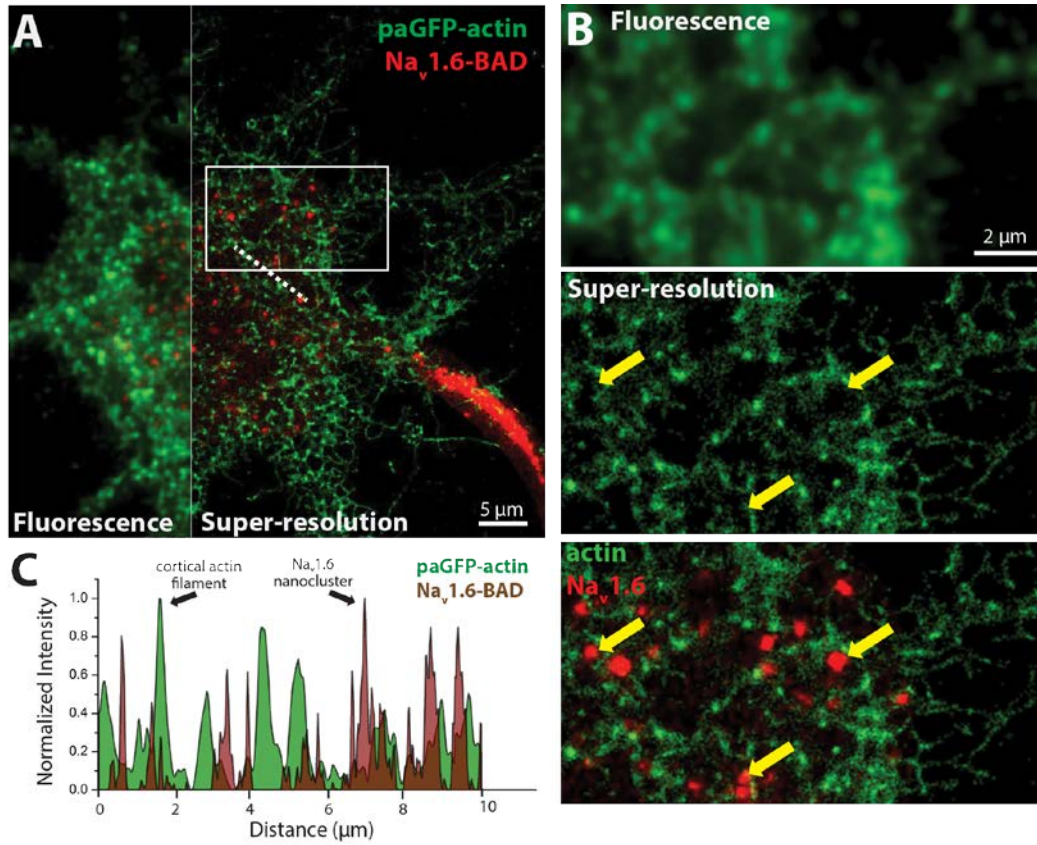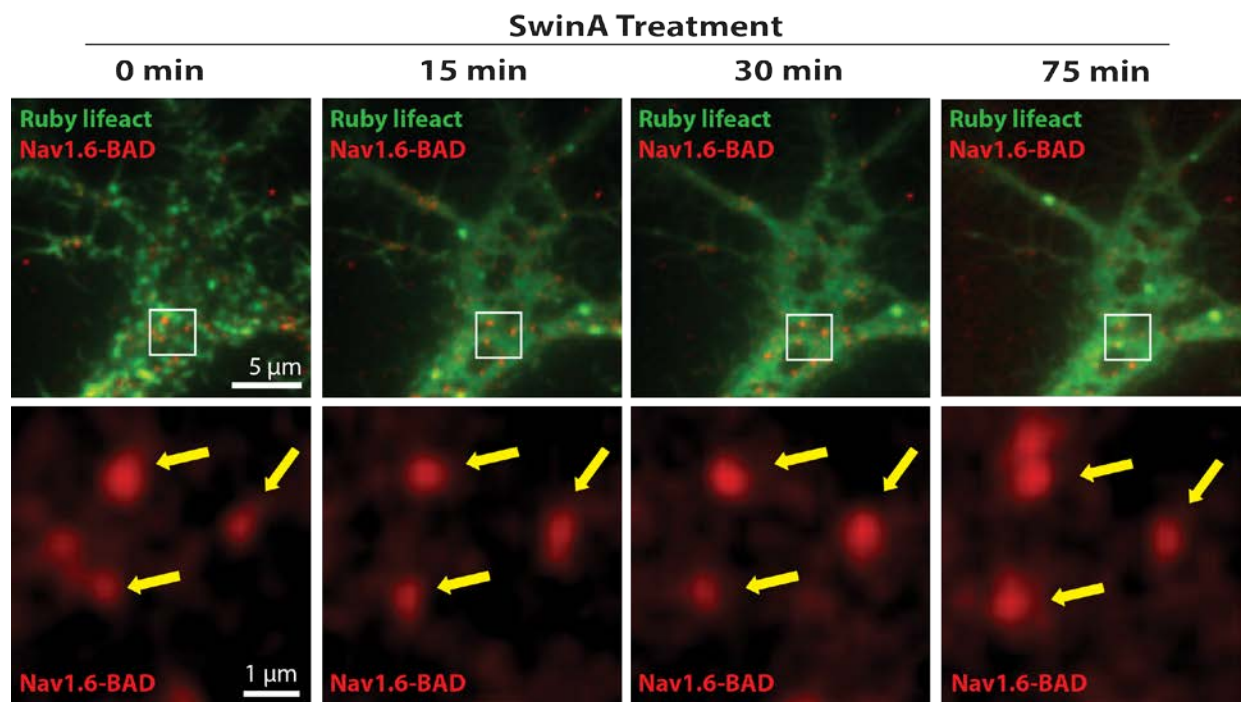
SUPPLEMENTARY FIGURE 2 Na$_v$1.6 nanoclusters are not associated with cortical actin.
(A) DIV10 rat hippocampal neuron transfected with photoactivatable-GFP-actin (paGFP-actin) and Na$_v$1.6-BAD. Surface distribution of Na$_v$1.6 visualized with CF640R. PALM-based super-resolution image of paGFP-actin (right side) was reconstructed from cycles of activation and photobleaching of individual paGFP-tagged actin molecules. The super-resolution image reveals fine actin structures not visible with light microscopy (left side). The single process with dense CF640 surface labeling is the axon initial segment. (B) Enlargement of white box in (A) showing the diffraction limited TIRF image of cortical actin (top panel), the paGFP-actin PALM reconstruction (middle panel) and an overlay of the Na$_v$1.6-BAD surface nanoclusters, visualized with CF640, with the paGFP-actin PALM reconstruction (bottom panel). (C) Line scan showing the normalized fluorescence intensity of actin (green) or Na$_v$1.6 (dark red) of the dotted white line in (A). Na$_v$1.6 nanoclusters (yellow arrows) are generally adjacent to, but not co-localized with cortical actin filaments.

To further address whether actin is involved in Na$_v$1.6 localization to nanoclusters, we imaged the distribution of Na$_v$1.6-BAD in the presence of 200 nM swinholideA (swinA), a drug that induces both f-actin depolymerization and depletion of G-actin. Fig. S3 shows a neuron

expressing Na$_v$1.6-BAD and Ruby-Lifeact, a fluorescent f-actin-binding peptide (3). The neuron was imaged in TIRF with a slow frame rate (once per min) to minimize photobleaching, and swinA was added after 10 min of imaging to establish a baseline. Fig. S3, top panels, show the imaging of Ruby-Lifeact and cell surface Na$_v$1.6-BAD following swinA addition. The change in Ruby-Lifeact fluorescence confirmed swinA-induced f-actin depolymerization. The bottom panels show an enlargement of the area denoted by the white box that contains three nanoclusters (yellow arrows) present before the addition of swinA. The location of the clusters remains remarkably consistent for 75 min after the addition of swinA.


SUPPLEMENTARY FIGURE 3 Actin depolymerization does not dissolve Na$_v$1.6 nanoclusters. A neuron expressing Na$_v$1.6-BAD and Ruby-Lifeact was imaged in TIRF. Na$_v$1.6-BAD was labeled with CF640 to visualize the surface distribution. The top panels illustrate the Ruby-Lifeact and Na$_v$1.6 nanocluster fluorescence in the presence of 200 nM swinA. The bottom panels show enlargements of the respective white boxes shown above, each containing three stable Na$_v$1.6 nanoclusters. Images were acquired once every min. The fluorescence intensity and location of the nanoclusters remained constant for more than 1 hour after actin depolymerization (yellow arrows). Ruby-Lifeact labeled actin filaments were used to demonstrate the effectiveness of swinA treatment.

Na$_v$1.6 nanoclusters do not colocalize with clathrin-coated pits, mitochondria or K$_v$2.1 induced ER-plasma membrane junctions

We next investigated colocalization of the Na$_v$1.6 nanoclusters with several scaffold/organelle markers. We first imaged clathrin-light-chain tagged with GFP (CLC-GFP) to determine whether the Na$_v$1.6 nanoclusters were formed via channel localization to endocytic sites (Fig. S4A). However, the surface Na$_v$1.6-BAD channels labeled with SA-CF640 did not co-localize with CLC-GFP. This result indicates that the nanoclusters are not endocytic platforms. This is consistent with the long lifetime seen for the nanoclusters since clathrin-coated pits tend to be transient (seconds to minutes) (4, 5). This does not exclude, however, that small numbers of Na$_v$1.6 channels could interact with clathrin since all proteins have a basal rate of protein turnover. Mitochondria localize near membrane-bound proteins and regulate them through calcium and oxidative signaling (6). Therefore, MitoTracker was used to identify mitochondria in live neurons and SA-488 was used to label the surface Na$_v$1.6-BAD. Mitochondria close to the plasma membrane were imaged in TIRF and compared to the distribution of Na$_v$1.6. No apparent relationship between mitochondria and the somatic nanoclusters was observed (Fig. S4B).

We next looked at the distribution of the Na$_v$1.6 nanoclusters in relation to the delayed rectifier K$_v$ channel, K$_v$2.1, which forms large micron-sized clusters on the soma and AIS of some neurons (7, 8). These channels were recently found to mediate the formation of junctions between the endoplasmic reticulum and plasma membrane (ER-PM junctions), which act as membrane trafficking hubs (9). We co-expressed Na$_v$1.6-BAD and GFP-K$_v$2.1, labeling surface Na$_v$1.6 with SA-594. Na$_v$1.6 nanoclusters were found around, but not within, large K$_v$2.1 clusters, as seen in Fig. S4C. This exclusion from K$_v$2.1-induced ER-PM junctions is likely due

to the large intracellular mass of the Na$_v$1.6 channel and may explain regions of soma membrane that were consistently devoid of Na$_v$1.6 single molecule tracks.
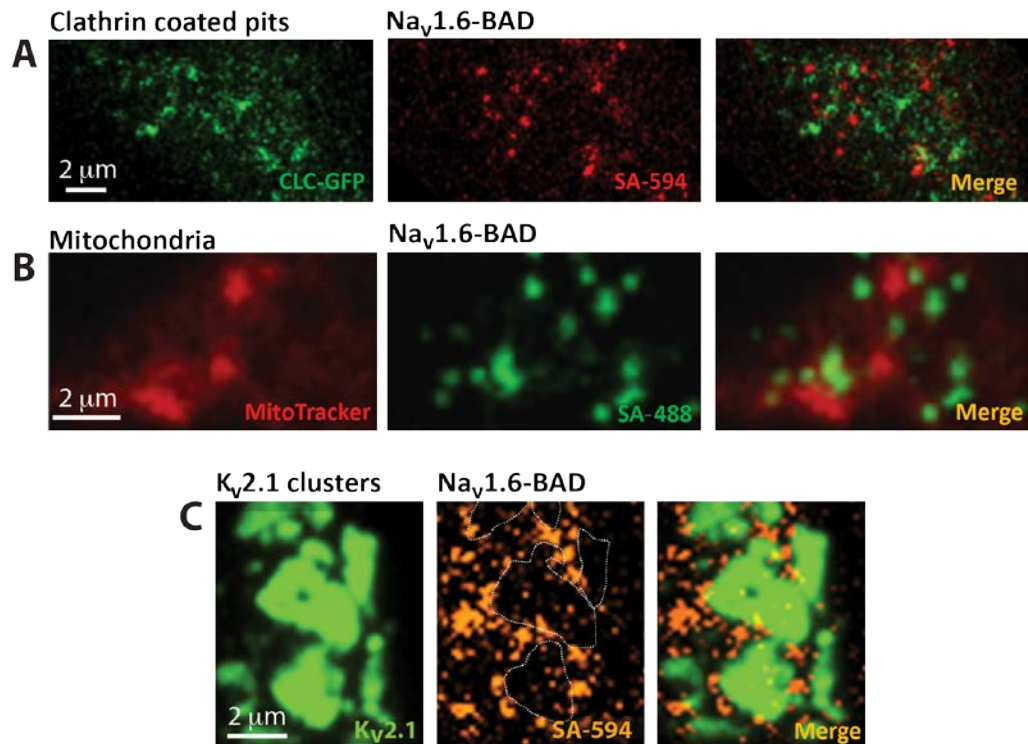
SUPPLEMENTARY FIGURE 4 Na$_v$1.6 clusters do not co-localize with endocytic sites, mitochondria or ER-PM junctions. (A) Neurons transfected with GFP-clathrin-light-chain (left green panel) and Na$_v$1.6-BAD labeled with SA-594 (red middle panel) show no significant co-localization as observed on the merge panel (right). (B) Mitochondria were labeled with MitoTracker (left panel, red) in live neurons transfected with Na$_v$1.6-BAD that was surface labeled in this case with SA-488 (middle panel, green). No apparent co-localization was observed. (C) Neurons co-transfected with GFP-K$_v$2.1, a marker of ER-PM junctions, (green) and Na$_v$1.6-BAD surface labeled with SA-594 (orange). The merged image of the two channels (right panel) shows how GFP-K$_v$2.1 (green) and Na$_v$1.6-BAD-SA594 (orange) localize to mutually exclusive regions, with Na$_v$1.6 nanoclusters located outside of the K$_v$2.1 clusters, and only few single channels located inside. All panels correspond to a somatic region of a neuron imaged in TIRF.

SUPPORTING REFERENCES

1. Ovesný, M., P. Křížek, J. Borkovec, Z. Švindrych, and G. M. Hagen. 2014. ThunderSTORM: a comprehensive ImageJ plug-in for PALM and STORM data analysis and super-resolution imaging. Bioinform. 30:2389-2390.

2. O'Connell, K. M., A. S. Rolig, J. D. Whitesell, and M. M. Tamkun. 2006. Kv2.1 potassium channels are retained within dynamic cell surface microdomains that are defined by a perimeter fence. J. Neurosci. 26:9609-9618.

3. Riedl, J., A. H. Crevenna, K. Kessenbrock, J. H. Yu, D. Neukirchen, M. Bista, F. Bradke, D. Jenne, T. A. Holak, and Z. Werb. 2008. Lifeact: a versatile marker to visualize F-actin. Nat. Methods 5:605-607.

4. Weigel, A. V., M. M. Tamkun, and D. Krapf. 2013. Quantifying the dynamic interactions between a clathrin-coated pit and cargo molecules. Proc. Natl. Acad. Sci. USA. 110:E4591-E4600.

5. Loerke, D., M. Mettlen, D. Yarar, K. Jaqaman, H. Jaqaman, G. Danuser, and S. L. Schmid. 2009. Cargo and dynamin regulate clathrin-coated pit maturation. PLoS Biology 7:e1000057.

6. Chaplin, N. L., M. Nieves-Cintrón, A. M. Fresquez, M. F. Navedo, and G. C. Amberg. 2015. Arterial smooth muscle mitochondria amplify hydrogen peroxide microdomains functionally coupled to L-type calcium channels. Circ. Res. 117:1013-1023.

7. Sarmiere, P. D., C. M. Weigle, and M. M. Tamkun. 2008. The K_v2.1 K^+ channel targets to the axon initial segment of hippocampal and cortical neurons in culture and in situ. BMC Neurosci. 9:112.

8. Tamkun, M. M., K. M. O'Connell, and A. S. Rolig. 2007. A cytoskeletal-based perimeter fence selectively corrals a sub-population of cell surface Kv2.1 channels. J. Cell Sci. 120:2413-2423.

9. Fox, P. D., C. J. Haberkorn, E. J. Akin, P. J. Seel, D. Krapf, and M. M. Tamkun. 2015. Induction of stable endoplasmic reticulum/plasma membrane junctions by K_v2.1 potassium channels. J. Cell Sci. 128:2096-2105.

MOVIE LEGENDS

MOVIE S1. Diffusion behavior of Nav1.6 channels on the somatic surface. Surface channels were labeled with SA-CF640R and imaged at 10 Hz using TIRF microscopy. The yellow arrows point to static nanoclusters while the white arrow points to a region that transiently accumulates individual channels.

MOVIE S2. Diffusion behavior of Nav1.6 channels on the glial cell surface. Surface channels

labeled with SA-CF640R were imaged at 10 Hz using TIRF microscopy.